JOURNAL OF AIRCRAFT
Vol. 31, No. 1, Jan.–Feb. 1994

# Effect of Canard Deflection on Close-Coupled Canard-Wing-Body Aerodynamics

Eugene L. Tu*
*NASA Ames Research Center, Moffett Field, California 94035*

**The thin-layer Navier-Stokes equations are solved for the flow about a canard-wing-body configuration at transonic Mach numbers of 0.85 and 0.90, angles of attack from −4 to 10 deg, and canard deflection angles from −10 to +10 deg. Effects of canard deflection on aerodynamic performance, including canard-wing vortex interaction, are investigated. Comparisons with experimental measurements of surface pressures, lift, drag, and pitching moments are made to verify the accuracy of the computations. The results of the study show that the deflected canard downwash not only influences the formation of the wing leading-edge vortex, but can cause the formation of an unfavorable vortex on the wing lower surface as well.**

## Introduction

MANY modern aircraft, both operational and experimental, utilize canards for maneuver control and improved aerodynamic performance. In addition to providing positive pitch control, influence of canards on wing aerodynamics can often result in increased maximum lift and decreased trim drag. Canard configurations have inherently different stability and trim characteristics from conventional tailplane configurations. However, with the capability of present-day automatic control systems, the reduced or even negative static stability of a canard configuration can lead to improved aircraft agility and maneuverability.

Aircraft using canards as primary pitch control surfaces often require large canard deflections. For example, the X-31 aircraft has a long-coupled canard which deflects between +20 and −70 deg for pitch and recovery control.[1] For closely coupled canards, a deflected canard has a more significant effect on the canard-wing aerodynamic interaction and, consequently, the aerodynamic performance of the aircraft. The NASA X-29, SAAB Viggen, and SAAB Gripen are three examples of fully integrated close-coupled canard configurations. The X-29 has a forward swept wing and a movable close-coupled canard which is the primary pitch control surface as well as an integral component in the active control system.[2] The Viggen has a close-coupled fixed canard for high-performance aerodynamics, while its successor, the Gripen, utilizes movable close-coupled canards to obtain maximum lift in maneuvering, maximum lift-to-drag ratio in cruise, and even nose-down pitching moment during short-field landing rollout.[3] Proper utilization of canards in present and future aircraft requires an accurate understanding of their influence on the flow structure about the wing.

At moderate angles of attack, for canards or wings with sharp leading edges, the flow separates at the leading edge due to the adverse pressure gradient on the leeward side. A free vortex sheet is formed which rolls up over the upper surfaces of the canard or wing. If the vortex is sufficiently strong, secondary, and in some cases, tertiary separations may result.

Received May 5, 1992; presented as Paper 92-2602 at the 10th AIAA Applied Aerodynamics Conference, Palo Alto, CA, June 22–24, 1992; revision received Nov. 20, 1992; accepted for publication Nov. 25, 1992. 

*Research Scientist, Computational Aerosciences Branch, M/S 258-1. Member AIAA.

The flow structure of highly swept or delta canard-wing configurations is characterized by a canard downwash which modifies the wing flowfield and an interaction between the canard and wing vortex systems. The inboard wing flowfield is often dominated by the canard downwash, and the outboard is affected by the subsequent change in wing leading-edge vortex formation and the canard-wing vortex interaction. Details of a typical coplanar canard-wing flow structure are given in Ref. 4. Deflecting the canard can drastically change the canard-wing aerodynamic interaction. For example, the stronger canard downwash and modified canard trailing-edge location of a positively deflected canard will significantly change the wing flowfield relative to that of the coplanar canard case.

Additional flow features contributing to the complex flow structure of deflected canard configurations in the transonic regime include secondary, trailing edge, and tip vortices, as well as regions of shock-induced or other boundary-layer separations. In addition to off-surface crossflow shocks, a strong primary vortex often causes the formation of a strong secondary vortex which significantly affects the surface pressures near the canard or wing leading edge. Furthermore, trailing-edge and tip vortices can interact with the leading-edge vortex as it convects downstream. If these vortices are formed on the canard, then further interaction with the wing vortex system occurs. The boundary-layer separation due to a high angle of attack, or induced by a strong recovery shock, is also influenced by the presence of these vortices.

The use of canards for improved performance has been supported by numerous experimental studies as well as some recent computational studies. Gloss and McKinney[5] and Gloss[6,7] provided insight into the effects of canard geometry and positioning on the aerodynamic loading of a typical canard-wing-body geometry. Lacey[8] conducted an extensive four-volume experimental study on the effects of canard geometry, position, and deflection on aerodynamic loads in the subsonic to supersonic regimes. A series of experimental studies by Gloss and Washburn[9–11] provided detailed measurements of surface pressures, as well as integrated force quantities on a variety of configurations and flow conditions near the transonic regime. More recent experimental studies[12–14] concentrated on the canard and wing vortex systems and provided details into the mechanisms of their interaction. In addition to canard sizing and positioning, Gloss et al.[15] and Dollyhigh[16] showed the effects of canard deflection on integrated forces and moments in the high subsonic and supersonic regimes, respectively. In the past, Refs. 8, 15, and 16 were some of the few detailed studies available on canard configurations with canards at various deflection angles. Recent experimental studies by Howard and Kersh[17] and Ponton et al.[18] have given detailed information on the flow structure of deflected canard geometries

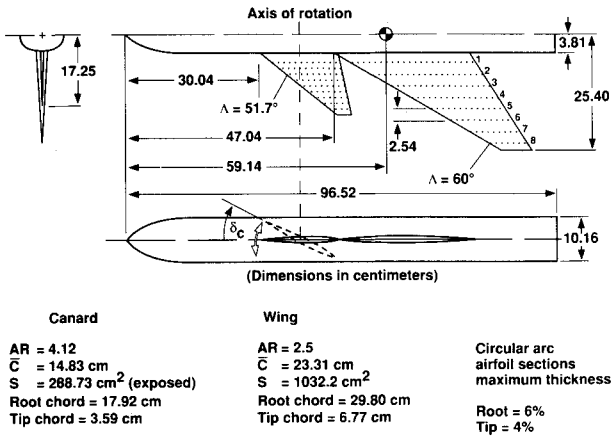


**Fig. 1 Canard-wing-body geometry; $\delta_c$ shown.**

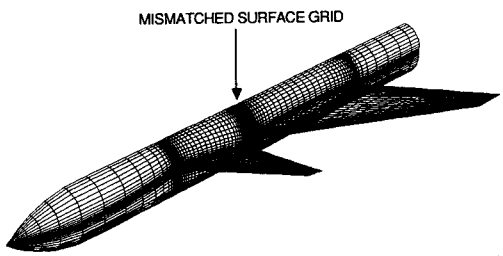


**Fig. 2 Surface grid for the deflected canard configuration ($\delta_c$ = 10.0 deg).**

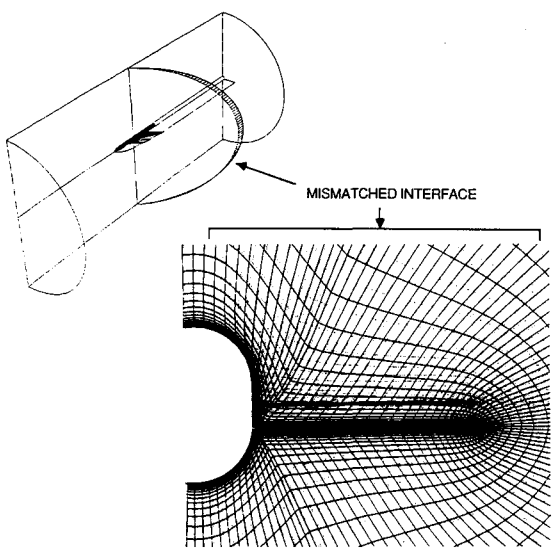


**Fig. 3 Canard-wing-body flowfield grid topology and canard/wing mismatched interface.**

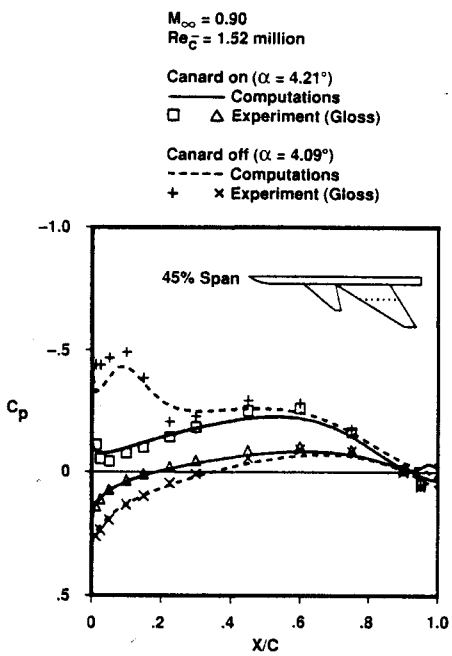


**Fig. 4 Comparison of computed and experimental surface pressure coefficients for the undeflected ($\delta_c$ = 0.0 deg) canard configuration with and without canard. $M_\infty$ = 0.90, $\alpha \approx$ 4 deg.**

in the low subsonic regime, and have shown encouraging results towards the optimization of such configurations.

Computational fluid dynamics (CFD) has become a valuable tool for understanding the complex three-dimensional flow physics of canard configurations. A number of studies based on conformal mapping, linear and nonlinear vortex lattice methods, the transonic small perturbation (TSP) equation, and Euler equations, have been performed and are listed in Ref. 4. However, to the author's knowledge, limited computational work to study canard-wing interaction has been performed using the Navier-Stokes (NS) equations, and even less work has been conducted using the NS equations to study the effects of deflected canards in detail. Although viscous computations are generally not required for sharp leading-edge-type separations, viscous modeling is essential to capture some of the other significant features of canard-wing aerodynamics, such as vortex-induced secondary separations, resulting secondary and tertiary vortices, and other boundary-layer-type separations. With the emergence of faster computers and increased memory capacities, the Navier-Stokes equations can now be utilized to study the complex flow structure of canard-wing-body aerodynamics.

Using an extension of the NASA Ames Research Center's Transonic Navier-Stokes (TNS) code,[19,20] the thin-layer Navier-Stokes equations are solved for the steady flow about a highly-swept canard-wing-body configuration, including canard deflection. A previous study[4] by the author confirmed the suitability of the present method for accurately simulating coplanar canard-wing-body aerodynamics. Accuracy was demonstrated by extensive comparisons with experimental measurements and a grid refinement study. In the present study, the aerodynamic characteristics of a deflected canard configuration, including the effects of canard deflection on the canard-wing leading-edge vortex interaction, are investigated. Comparisons with available experimental data for the deflected canard cases are used to validate the extension of the code. This current application of the TNS code expands the capability for analysis of the complex aerodynamics of general canard configurations.

## Computational Modeling

### Numerical Procedure

The TNS code is a Reynolds-averaged thin-layer Navier-Stokes solver with structured zoning capability, and has been demonstrated for a wide range of wing and aircraft configurations.[4,19-23] The original four-zone version of the TNS wing code has been used to solve for and investigate transonic viscous flows over various wing geometries with and without wind-tunnel wall modeling.[19,21] The 16- and 27-zone versions of the TNS wing-fuselage (TNSWF) code have been successfully used to compute the flow about a modified F-16A wing-fuselage configuration[22] and a complete F-16A aircraft,[23] respectively. The code used in this study is a generalized version of the TNS code without restriction on grid topology or zonal

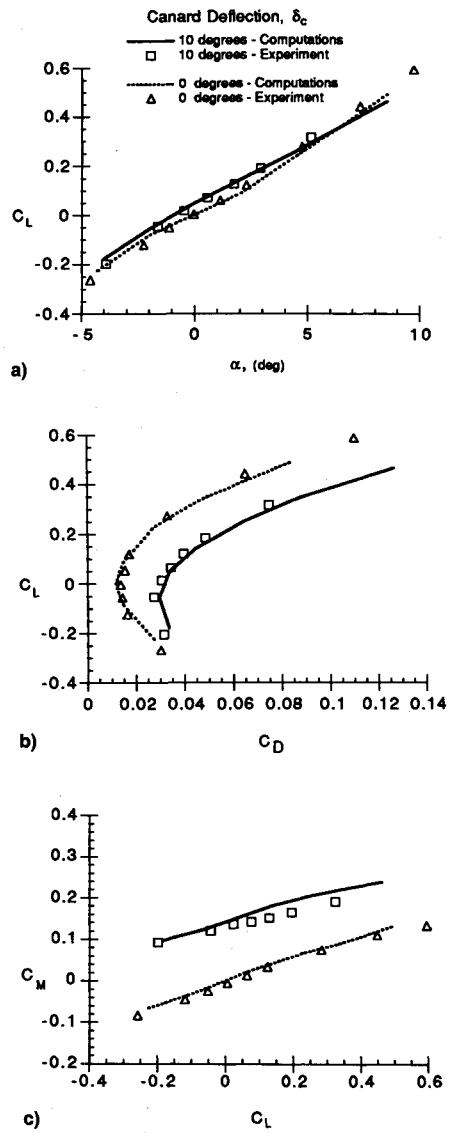


**Fig. 5 Comparison of computed and experimental forces and moments for the undeflected ($\delta_c$ = 0.0 deg) and deflected ($\delta_c$ = 10.0 deg) canard configurations. $M_\infty$ = 0.85: a) lift curves, b) drag polars, and c) moment curves.**

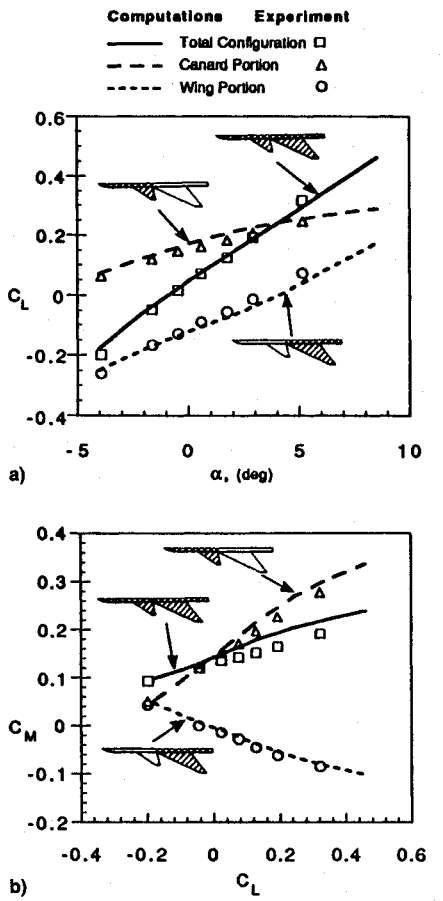


**Fig. 6 Comparison of component lift and pitching moment curves for the deflected canard configuration at $\delta_c$ = 10.0 deg. $M_\infty$ = 0.85: a) lift and b) moment.**

arrangement. For applications to deflected close-coupled canard configurations, the TNS code has been further extended to allow for mismatched patched interfaces.

Since the TNS code solves the Reynolds- (or time-) averaged equations, the Baldwin-Lomax algebraic eddy-viscosity model[24] is chosen to compute the effects of turbulence on the flow. Due to the vortex-dominated flow structures of the highly swept sharp leading-edge canard and wing, a modification to the original Baldwin-Lomax formulation is required. Without such a modification, the author has found that the level of turbulent viscosity predicted by the Baldwin-Lomax model is incorrectly influenced by the canard and wing vortices. For this study, the Degani-Schiff modification,[25] as originally developed for crossflow-type separations, is employed. It is noted that with present-day CFD technology, higher-order eddy-viscosity models could easily be utilized and are readily available within the TNS code. However, with the lack of significant nonequilibrium effects anticipated and the moderate angles of attack being investigated, the benefits for the current study of such higher-order models do not justify the increased computational costs. Further details about the TNS code, algorithm, zonal approach, and general performance are given in Refs. 19–21.

All results were computed using the supercomputer facilities at NASA Ames Research Center. A typical case required 3000 iterations from freestream conditions to converge, as defined by a three-order drop in residuals (L2 norm), stable configuration forces, and stable wing surface pressure distributions. Less than 1000 iterations were required for restart cases with perturbations in angle of attack, Mach number, or Reynolds number.

### Geometry Modeling and Grid Generation

The geometry in this study is based on the wind-tunnel model used by Gloss et al.,[6,9–11,15] and is illustrated in Fig. 1. In the wind-tunnel model, fairings were used to facilitate a vertical offset canard. These fairings, which account for slight asymmetries in the experimental results, are omitted in the current computational modeling. The deflected canard rotates about the spanwise axis (perpendicular to the symmetry plane) at the midcanard-root location as shown. For the swept canard, deflection results in pure rotation at the canard root section and a combination of translation and rotation at the canard tip. The cross-sectional shape of the body allows for a +10- to −10-deg canard deflection without a canard-root/body gap. Canard deflection angles $\delta_c$ are given relative to the body axis (or wing position), with positive $\delta_c$ representing higher canard angles of attack $\alpha_c$. The $\delta_c$ = 0.0-deg canard deflection represents the coplanar canard case. The sting used for wind-tunnel mounting is modeled by extending the body, with its appropriate no-slip boundary condition, to the downstream boundary. In order to compare with the experimental data,[6] integrated force and moment results are given for the configuration without the sting, and the drag coefficients are given assuming a condition of freestream static pressure on the base area of the model.

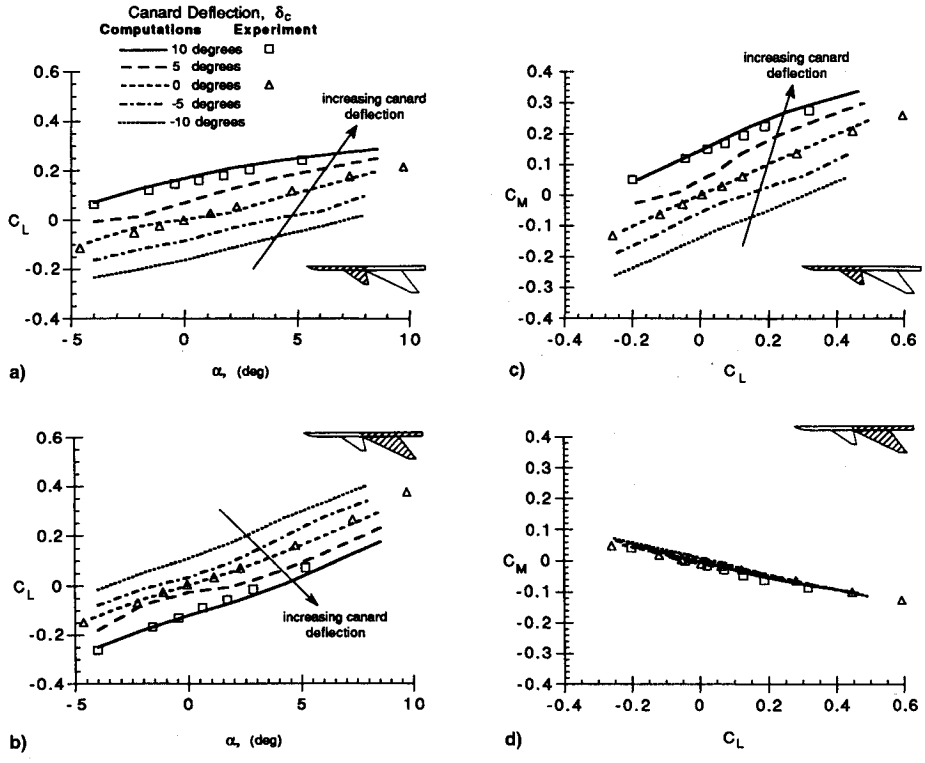


**Fig. 7 Effect of $\delta_c$ on wing and canard portion lift and moment curves. $M_\infty = 0.85$: a) canard portion lift, b) wing portion lift, c) canard portion moment, and d) wing portion moment.**

Using the S3D surface geometry and surface grid generation code,[26] the canard, wing, and body component surface geometries are modeled from their original analytical definitions. S3D is first used to generate the coplanar (undeflected) case, and an algebraic redistribution of the surface grid combined with cubic spline interpolation is then used for the deflected canard cases. Only the canard portion (canard plus forebody) of the surface grid is modified for the deflected canard cases. It is emphasized that for the current computations, the deflected canard is actually rotated (not sheared) about the midcanard-root spanwise axis. An example of the surface grid for the deflected canard case is shown in Fig. 2. The redistribution of the surface grid is performed as follows: 1) the canard points are rotated about the specified axis; 2) the upper/lower body dividing line forward of the canard is assumed to be parabolic; 3) the axial distribution of the body cross sections is adjusted according to the rotated canard; and 4) the points along each cross section are redistributed using cubic spline interpolation based on the new arc length of each section.

Figure 2 shows that a mismatch in the surface grid is produced on the body at the canard-wing junction. Consequently, there is a mismatch in the zonal interface separating the canard and wing portions of the flowfield grid. The 3DGRAPE[27] program is used to generate the coplanar canard and wing portions of the flowfield grid individually with a mutual overlapping interface analytically defined. In order to resolve the viscous boundary layer near the canard, wing, and body surfaces, an average value of $y^+ < 5$ was achieved by clustering the flowfield grid to the surface (average first grid spacing is approximately $10^{-5}\bar{c}$).

In a manner similar to the surface grid, the flowfield grids for the deflected canard cases are generated using an algebraic redistribution of the original elliptically generated coplanar canard-wing-body grid. By using this technique for both the surface and flowfield grids, the grids for any $\delta_c$ can be efficiently obtained.

The overall H-O topology grid, with the mismatched interface, for a typical deflected canard case ($\delta_c = 10$ deg) is shown in Fig. 3. An expanded crossflow plane view of the interface is also shown with the solid grid indicating the downstream boundary of the canard portion grid. Since the mismatched interface surface is not necessarily a plane, trilinear interpolation as formulated in Ref. 28 is used to transfer flow quantities from one zone to the other. For all of the cases presented in this study, the nonconservative form of interpolation is used. Accuracy was determined by comparing the solution from a single-block (conservative) coplanar canard case with the solution from a multiblock mismatched-interface (nonconservative) coplanar canard case. Differences in surface and flowfield pressure contours between the two test cases were negligibly small.

The resulting grid for a deflected canard case contains 9400 points on the surface (total for half-model) and 590,000 flowfield points. Up to six zones stacked in the streamwise direction are used to minimize core memory requirements. Except for the canard/wing portion interface, one-to-one grid matching is used on all interfaces. Since the current computations are performed in the transonic regime, the flowfield grid is extended upstream and downstream by approximately eight wing root-chord lengths, and in the radial direction by six wingspan lengths.

## Results and Discussion

### Experimental Comparisons

Comparisons between computed results and experimental data[6,9-11,15] are made to validate the current method for accurately predicting the steady flowfield of deflected canard cases. All computations are at transonic Mach numbers $M_\infty$ of 0.85 and 0.90, angles of attack $\alpha$ ranging from $-4$ to $+10$ deg, and $\delta_c$ from $-10$ to $+10$ deg. To match experimental conditions, at $M_\infty = 0.85$ and 0.90, the Reynolds number based on the mean aerodynamic chord of the wing $Re_{\bar{c}}$ is 2.82 and 1.52 million, respectively. Transition strips were used in the experiments at the body nose and leading edges of the canard and wing. Therefore, the computations are performed assuming fully turbulent flow.

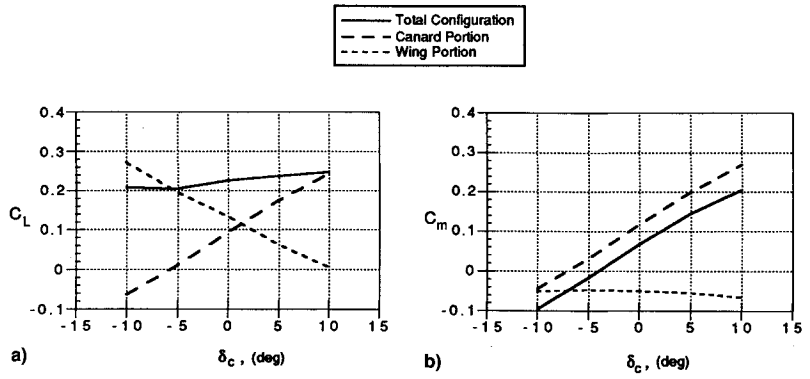


**Fig. 8 Effect of $\delta_c$ on component lifts and pitching moments at $M_\infty = 0.85$ and $\alpha = 4.27$ deg: a) lift and b) moment.**

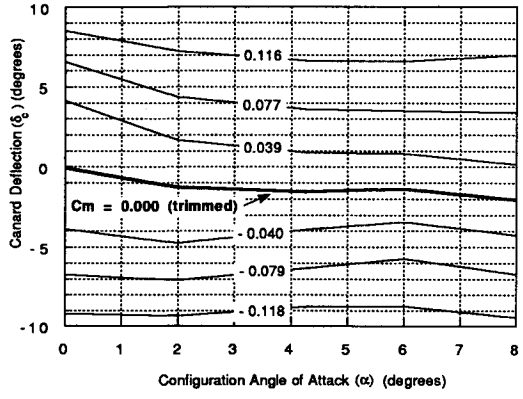


**Fig. 9 Contour plot of computed total pitching moment at $M_\infty = 0.85$ with moment center at c.g. location (59.14 cm from nose).**

Figure 4 shows the effect of an undeflected canard on the wing flowfield at an inboard wing span station of 45% for $M_\infty = 0.90$ and $\alpha \approx 4$ deg. This is the only case in the current study for which experimental surface pressure data[10] is available. For all deflected or noncoplanar canard cases, only integrated force and moment experimental data[15] are available. The inboard station of the wing is significantly influenced by the presence of the canard. For the canard-off case, the suction peak on the upper surface identifying the presence of a leading-edge vortex is clearly evident. At this angle of attack, the canard-on results show that the formation of the wing leading-edge vortex is inhibited at the inner station. This effect of the canard on the leading-edge vortex is directly attributed to the canard downwash. At higher angles of attack, more extensive coplanar canard results[4] show that the wing leading-edge vortex is weakened at the inboard stations, and a significant canard-wing vortex interaction occurs at the outboard stations. The results presented in Ref. 4 also show that the minor discrepancy between the computational and experimental results in Fig. 4, particularly in resolution of the vortex strength, is essentially resolved with grid refinement. For the current study, such grid refinement is deemed unnecessary for the accuracy required.

Comparisons of the computed lift, drag, and pitching moment curves with experimental data[15] are given in Fig. 5 for $\delta_c$ of 0 and 10 deg. In order to match with experimental test conditions, the computations performed for Fig. 5 and all subsequent figures are at $M_\infty = 0.85$ and $Re_{\bar{c}} = 2.82$ million. Figure 5a shows the nonlinearity in the lift curves. Note that the subtle differences in the experimental $\delta_c = 0$-deg and $\delta_c = 10$-deg lift curves are captured well by the computations. The drag polar curves in Fig. 5b show that the undeflected canard ($\delta_c = 0.0$ deg) exhibits a lower overall drag coefficient $C_D$. The drag polars also show that minimum $C_D$ for the 10-deg case occurs at a negative lift coefficient $C_L$. Figure 5c shows that increasing canard deflection increases overall

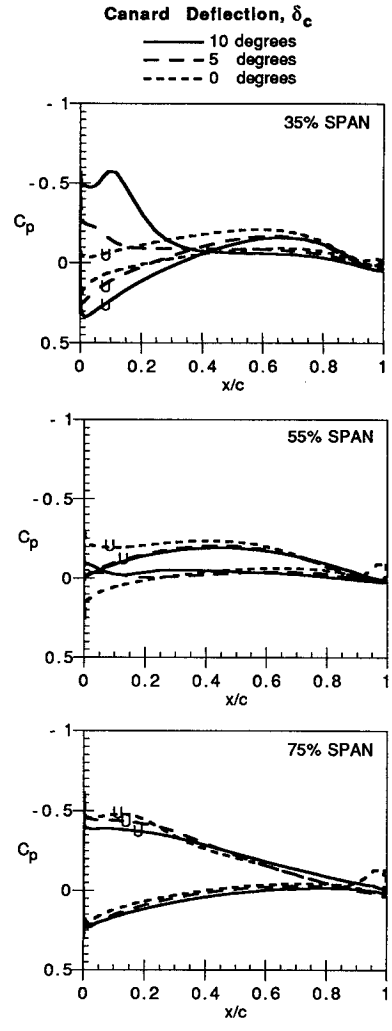


**Fig. 10 Effect of $\delta_c$ on wing surface pressures at $M_\infty = 0.85$ and $\alpha = 4.27$ deg. (Upper surface pressures indicated by $U$.)**

pitching moments for all computed angles of attack. For these results, the moment center is located at 63.17 cm from the nose (slightly aft of the model c.g. at 59.14 cm shown in Fig. 1). Significant nonlinearities due to the canard-wing interaction are also noted in the pitching moment curves.

In order to examine the effects of canard deflection in more detail, the lift and pitching moment curves are separated into two configuration component regions. The canard region consists of the canard and the body forward of the wing leading-edge root location (forebody). The wing region consists of the wing and the remaining aft-body (not including the sting). Figures 6a and 6b illustrate lifts and moments, respectively,

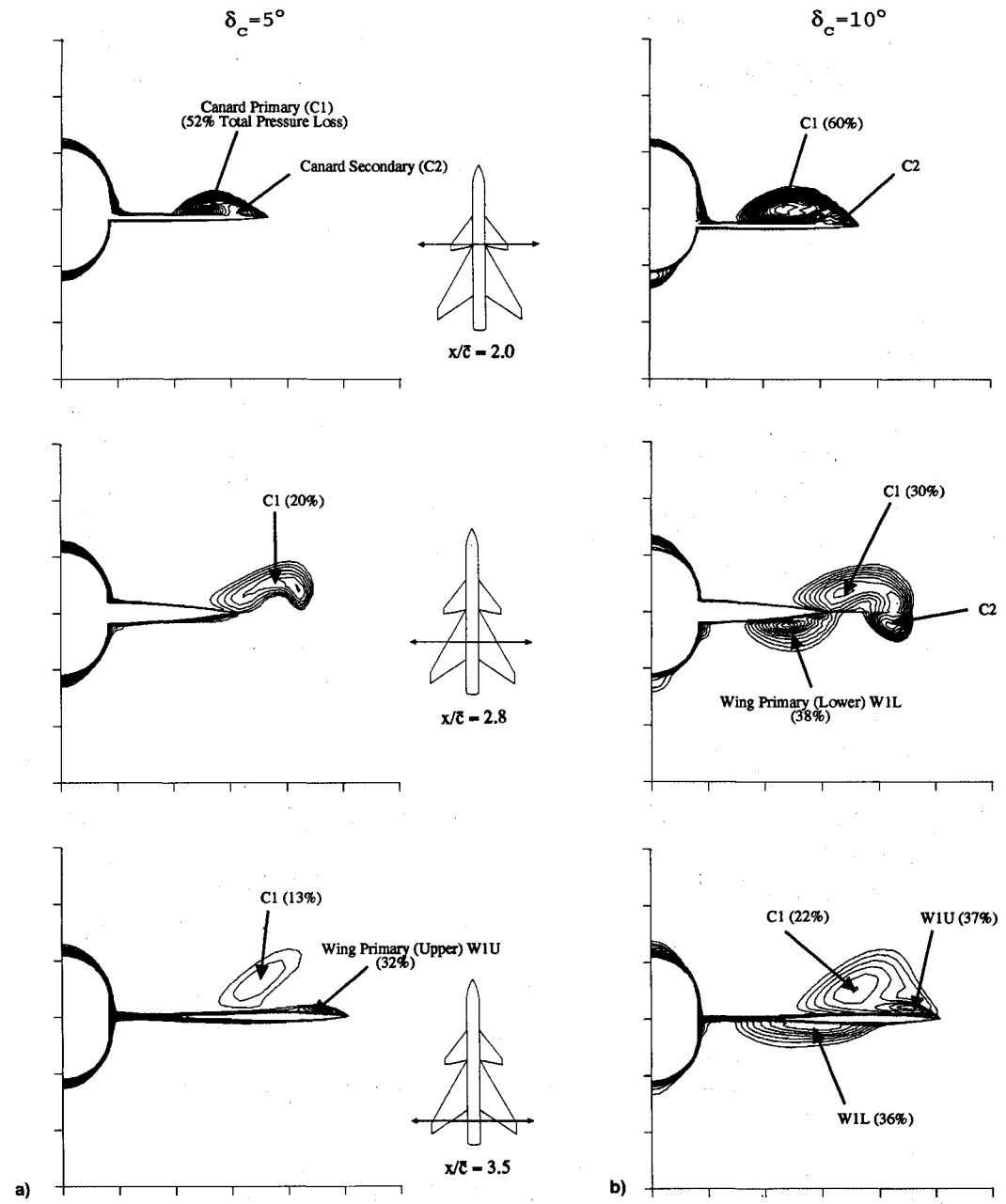


**Fig. 11 Crossflow plane visualization of normalized total pressure contours for canard deflections of $\delta_c$ = 5 and 10 deg. $M_\infty$ = 0.85, $\alpha$ = 4.27 deg.**

for the $\delta_c$ = 10-deg case. The wing portion lift curve of Fig. 6a shows the effect of the canard downwash on reducing wing lift. For example, at $\alpha$ = 0 deg, the additional canard lift (due to its deflection) is mostly cancelled by the negative lift generated by the wing (due to the canard downwash). The pitching moment curves in Fig. 6b show that the wing, in the presence of the canard, exhibits statically stable characteristics, while the canard pitching moment causes the total configuration to be statically unstable. Such characteristics are often typical of canard configured aircraft. Favorable comparisons in Figs. 6a and 6b between computations and experimental data indicate that the distribution of lift and moment between the component regions are captured well by the computations.

### Effect of Canard Deflection

*Integrated Forces and Moments*

An analysis of the effect of canard deflection on lift, pitching moment and, particularly, trimmed conditions, is given in this section. For long-coupled canard configurations, the effect on aerodynamic performance is usually limited to the lift of the canard itself and the total pitching moment. However, the close-coupled canard, by definition, has significant influences on wing performance.

Figure 7 shows lift and moment curves for the canard and wing portions at various $\delta_c$, ranging from $-10$ to $+10$ deg. While the canard portion lift curve (Fig. 7a) exhibits increasing lift for increasing $\delta_c$ at a given $\alpha$, the wing portion lift curve (Fig. 7b) decreases for increasing $\delta_c$. As $\delta_c$ is increased, the canard generates greater lift and, consequently, greater downwash in the canard wake. The resulting effective wing angle of attack $\alpha_w$ on the inboard portion of the wing decreases with increasing $\delta_c$. Vortex visualization results presented later in this article will show that, for certain $\alpha$ and $\delta_c$ values, $\alpha_w$ can be negative in the inboard wing while freestream $\alpha$ is positive.

The canard and wing portion pitching moment curves for various canard deflection angles are given in Figs. 7c and 7d, respectively. The canard portion pitching moment increases

as $\delta_c$ is increased, while the wing portion pitching moment is relatively insensitive to $\delta_c$. The strong $\delta_c$ coupling with wing portion lift (Fig. 7b) and the weak coupling with wing moment (Fig. 7d), indicate a significant shift in wing c.p. as a function of $\delta_c$.

Figure 8 illustrates lift and moment as a function of $\delta_c$ at a representative $\alpha$ of 4.27 deg. The lift curves in Fig. 8a are given for the total configuration, canard portion, and wing portion. For increasing $\delta_c$, the cancellation of the lift between the canard and wing portions is clearly observed. At this moderate angle of attack, the total lift is minimally affected by the deflection of the canard. The moment curves in Fig. 8b show that the canard portion moment is the major contributor to changes in the total configuration moment. At this condition ($M_\infty = 0.85$, $\alpha = 4.27$ deg), the configuration is trimmed about 69.17 cm from the nose at $\delta_c \approx -4$ deg.

For a realistic aircraft configuration, the determination of trimmed lift and drag is critical in assessing aerodynamic performance. A contour plot of pitching moment about the model c.g. location (59.14 cm from the nose) is given in Fig. 9. The trimmed ($C_m = 0.0$) pitching moment curve is highlighted, and indicates that relatively small negative canard deflections are required to trim this configuration at moderate angles of attack.

*Canard-Wing Vortex Interaction*

For the current configuration, the primary mechanism for the canard-wing aerodynamic interaction is the canard's influence on the wing leading-edge vortex system. Both the canard downwash and the canard leading-edge vortex have pronounced effects on the formation and trajectory of the wing vortex. At given angles of attack, the additional freedom-of-motion of canard deflections allows for widely varying types of wing vortex structures. In addition to the strength of the canard downwash, changing $\delta_c$ affects the strength of the canard vortex, the location of the canard trailing-edge relative to the wing, and the subsequent canard vortex trajectory in the wing flowfield. The following flow visualization figures are given for $M_\infty = 0.85$ and $\alpha = 4.27$ deg.

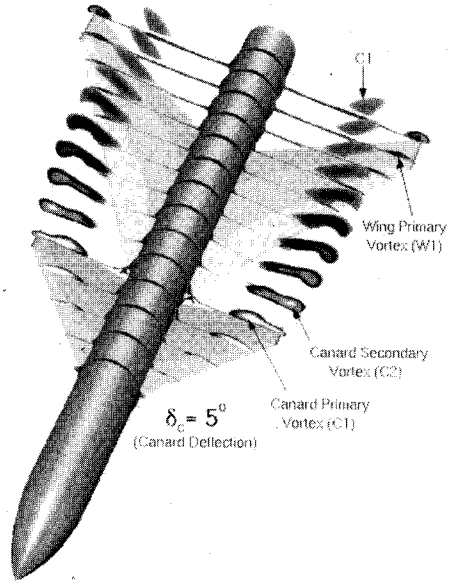


**Fig. 12 Perspective view of upper surface canard-wing vortex structure for canard deflection of $\delta_c = 5$ deg. $M_\infty = 0.85$, $\alpha = 4.27$ deg.**

Figure 10 illustrates the effect of canard deflection on wing surface pressure at 35, 55, and 75% span. For clarity, the upper surface pressure curves are indicated ($U$). As canard deflection is increased from 0 to 10 deg, the leading-edge lower surface pressure at 35% span transitions from positive to negative values. At $\delta_c = 10$ deg, a strong suction peak exists on the lower surface, indicating the possibility of a wing vortex on the wing lower surface. Towards the outboard stations, the effect of canard deflection on surface pressure is minimal.

To visualize the effect of canard deflection on the canard-wing vortex interaction, crossflow contours of total stagnation pressures are given in Fig. 11 for $\delta_c = 5$ and 10 deg. The crossflow contours are shown at $x/\bar{c} = 2.0$, 2.8, and 3.5, as measured from the fuselage nose. The relative primary vortex strengths are indicated in the figure by the approximate total pressure loss in the vortex core. For $\delta_c = 5$ deg (Fig. 11a), there are canard primary (C1), canard secondary (C2), and wing primary (W1U) vortices over the upper surfaces of the canard and wing. The distortion of the canard primary vortex at $x/\bar{c} = 2.8$ is due, in part, to the canard secondary vortex.

At $\delta_c = 10$ deg (Fig. 11b), an additional wing primary vortex (W1L) forms and is visible on the wing lower surface ($x/\bar{c} = 2.8$). This vortex causes the suction peak on the lower surface of the wing observed earlier in Fig. 10, and would generally be considered an unfavorable effect. At these flow conditions, there is a transition from negative to positive $\alpha_w$ from the wing-root to wing-tip locations. At the last station, $x/\bar{c} = 3.5$, the wing flowfield structure for the $\delta_c = 10$-deg case includes two wing primary vortices (upper and lower) as well as the canard primary vortex.

The mutual interaction between these vortices is an important factor in wing performance and is complex in nature. A comparison of the relative position of the canard vortex between $x/\bar{c} = 2.8$ and 3.5 in Fig. 11 shows that the trajectory of the canard vortex is influenced by the wing upper-surface vortex. For two corotating vortices (canard and wing primary), each with a position and counterclockwise rotation as shown in the figure, the wing vortex induces a relative inward motion of the canard vortex.

The influence of the wing vortex on the canard vortex trajectory is more clearly visualized in Fig. 12, which illustrates

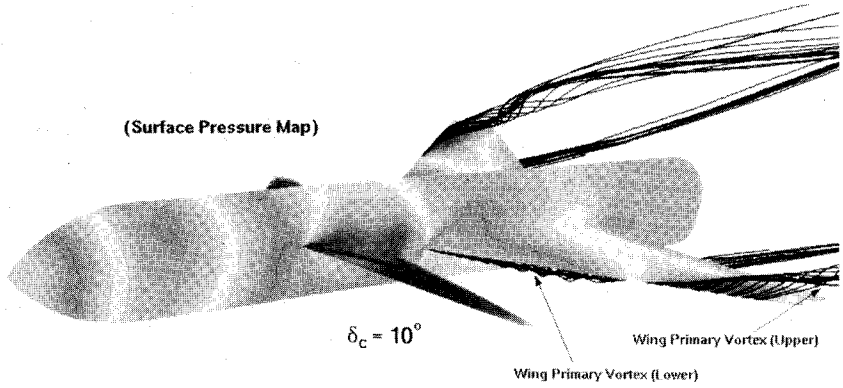


**Fig. 13 Perspective view of computed surface pressures and simulated particle traces for $\delta_c = 10$ deg. $M_\infty = 0.85$, $\alpha = 4.27$ deg.**

the upper surface canard and wing vortex systems for $\delta_c = 5$ deg. Crossflow contours of total stagnation pressure are shown at selected streamwise stations. At $\delta_c = 5$ deg, the formation of the wing vortex on the wing upper surface is inhibited by the canard downwash until outboard of the canard-tip span location. Figure 12 also shows that as the canard primary vortex is convected over the wing upper surface, the wing primary vortex in the outboard region clearly modifies the canard vortex trajectory inward.

Figure 13 shows a perspective view of the overall flowfield for the configuration at $\alpha = 4.27$ deg, and a higher canard deflection of $\delta_c = 10$ deg. The darker region over the canard upper surface indicates low pressure induced by the canard vortex. The particle traces released near the wing root and towards the wing tip, show the formation of the leading-edge vortices on the lower and upper surfaces. The wing vortex on the lower surface forms near the wing apex and is fed by the free vortex sheet from the inboard-wing leading edge. Toward the outboard wing, as $\alpha_w$ transitions from negative to positive values, the lower vortex is convected downstream and the upper vortex forms.

## Concluding Remarks

A numerical investigation of canard-wing aerodynamic interaction, including effects of canard deflections, has been performed. An efficient grid generation procedure, coupled with a thin-layer Reynolds-averaged Navier-Stokes solver, allows for the computations of any deflected canard cases with $\delta_c$ between $-10$ and $+10$ deg. Solution accuracy has been demonstrated by favorable comparisons with experimental data. The results show a pronounced effect of the deflected canard on aerodynamic performance parameters, particularly wing lift and configuration pitching moment. For the current close-coupled canard geometry, small canard deflections are required to trim the configuration.

Visualization of the canard-wing-body flowfield shows a complex flow structure consisting of several interacting canard and wing vortices. Specifically, at significantly large canard deflection angles, effective wing angle-of-attack transitions from negative (inboard) to positive (outboard) values causing the formation of both lower and upper surface leading-edge vortices. Furthermore, due to the strength of these vortices, secondary vortices are present, indicating strong viscous effects. Accurate prediction of such effects are needed in the design and optimization of future close-coupled canard aircraft.

## Acknowledgment

The author would like to thank Goetz Klopfer of MCAT Institute, San Jose, CA, for his helpful suggestions and discussions on the mismatched zoning scheme.

## References

[1]Yeh, D. T., George, M. W., Clever, W. C., Tam, C. K., and Woan, C. J., "Numerical Study of the X-31 High Angle-of-Attack Flow Characteristics," AIAA Paper 91-1630, June 1991.

[2]Kehoe, M. W., Bjarke, L. J., and Laurie, E. J., "An In-Flight Interaction of the X-29A Canard and Flight Control System," NASA TM 101718, April 1990.

[3]Modin, K. E., and Clareus, U., "Aerodynamic Design Evolution of the SAAB JAS 39 Gripen Aircraft," AIAA Paper 91-3195, Sept. 1991.

[4]Tu, E. L., "Navier-Stokes Simulation of a Close-Coupled Canard-Wing-Body Configuration," *Journal of Aircraft*, Vol. 29, No. 5, 1992, pp. 830–838.

[5]Gloss, B. B., and McKinney, L. W., "Canard-Wing Lift Interference Related to Maneuvering Aircraft at Subsonic Speeds," NASA TM X-2897, Dec. 1973.

[6]Gloss, B. B., "Effect of Canard Location and Size on Canard-Wing Interference and Aerodynamic-Center Shift Related to Maneuvering Aircraft at Transonic Speeds," NASA TN D-7505, June 1974.

[7]Gloss, B. B., "Effect of Wing Planform and Canard Location and Geometry on the Longitudinal Aerodynamic Characteristics of a Close-Coupled Canard Wing Model at Subsonic Speeds," NASA TN D-7910, June 1975.

[8]Lacey, D. W., "Aerodynamic Characteristics of the Close-Coupled Canard as Applied to Low-to-Moderate Swept Wings, Volumes 1–4," David W. Taylor Naval Ship Research and Development Center Rept. DTNSWDC-79/001-004, Jan. 1979.

[9]Gloss, B. B., and Washburn, K. E., "Load Distribution on a Close-Coupled Wing Canard at Transonic Speeds," *Journal of Aircraft*, Vol. 15, No. 4, 1978, pp. 234–239.

[10]Washburn, K. E., and Gloss, B. B., "Aerodynamic Load Distributions at Transonic Speeds for a Close-Coupled Wing-Canard Configuration: Tabulated Pressure Data," NASA TM 78780, Oct. 1978.

[11]Gloss, B. B., and Washburn, K. E., "A Study of Canard-Wing Interference Using Experimental Pressure Data at Transonic Speeds," NASA TP 1355, Jan. 1979.

[12]Er-El, J., and Seginer, A., "Vortex Trajectories and Breakdown on Wing-Canard Configurations," *Journal of Aircraft*, Vol. 22, No. 8, 1985, pp. 641–648.

[13]Calarese, W., "Vortex Interaction on a Canard-Wing Configuration," Air Force Wright Aeronautical Lab. TR-86-3100, Wright-Patterson AFB, OH, Oct. 1986.

[14]Oelker, H., and Hummel, D., "Investigations on the Vorticity Sheets of a Close-Coupled Delta-Canard Configuration," *Journal of Aircraft*, Vol. 26, No. 7, 1989, pp. 657–666.

[15]Gloss, B. B., Ray, E. J., and Washburn, K. E., "Effect of Canard Vertical Location, Size, and Deflection on Canard-Wing Interference at Subsonic Speeds," NASA TM 78790, Dec. 1978.

[16]Dollyhigh, S. M., "Static Longitudinal Aerodynamic Characteristics of Close-Coupled Wing-Canard Configurations at Mach Numbers from 1.60 to 2.86," NASA TN D-6597, Dec. 1971.

[17]Howard, R. M., and Kersh, J. M., Jr., "Effect of Canard Deflection on Enhanced Lift for a Close-Coupled-Canard Configuration," AIAA Paper 91-3222-CP, Sept. 1991.

[18]Ponton, A. J., Lowson, M. V., and Barrett, R. V., "The Evaluation of Canard Couplings at High Angles of Attack," AIAA Paper 92-0281, Jan. 1992.

[19]Holst, T. L., Kaynak, U., Gundy, K. L., Thomas, S. D., and Flores, J., "Numerical Solution of Transonic Wing Flows Using an Euler/Navier-Stokes Zonal Approach," *Journal of Aircraft*, Vol. 24, No. 1, 1987, pp. 17–24.

[20]Flores, J., "Convergence Acceleration for a Three-Dimensional Euler/Navier-Stokes Zonal Approach," *AIAA Journal*, Vol. 24, No. 9, 1986, pp. 1441, 1442.

[21]Kaynak, U., Holst, T. L., and Cantwell, B. J., "Computation of Transonic Separated Wing Flows Using an Euler/Navier-Stokes Zonal Approach," NASA TM 88311, July 1986.

[22]Flores, J., Reznick, S. G., Holst, T. L., and Gundy, K. L., "Transonic Navier-Stokes Solutions for a Fighter-Like Configuration," *Journal of Aircraft*, Vol. 25, No. 10, 1988, pp. 875–881.

[23]Flores, J., and Chaderjian, N., "Zonal Navier-Stokes Methodology for Flow Simulation About a Complete Aircraft," *Journal of Aircraft*, Vol. 27, No. 7, 1990, pp. 583–590.

[24]Baldwin, B. S., and Lomax, H., "Thin Layer Approximation and Algebraic Model for Separated Turbulent Flows," AIAA Paper 78-257, Jan. 1978.

[25]Degani, D., and Schiff, L. B., "Computation of Turbulent Supersonic Flows Around Pointed Bodies Having Crossflow Separation," *Journal of Computational Physics*, 66, 1986, pp. 173–196.

[26]Luh, R. C., Pierce, L., and Yip, D., "Interactive Surface Grid Generation," AIAA Paper 91-0796, Jan. 1991.

[27]Sorenson, R. L., "The 3DGRAPE Book: Theory, Users' Manual, Examples," NASA TM 102224, July 1989.

[28]Klopfer, G. H., and Molvik, G. A., "Conservative Multizone Interface Algorithm for the 3-D Navier-Stokes Equations," AIAA Paper 91-1601, June 1991.